Large-Scale Production of Size-Controlled MoS$_2$ Nanosheets by Shear Exfoliation

Eswaraiah Varrla,[†,§] Claudia Backes,[†,§] Keith R. Paton,[†,‡] Andrew Harvey,[†,§] Zahra Gholamvand,[†,§] Joe McCauley,[§] and Jonathan N. Coleman*[,†,§]

†CRANN and AMBER Research Centres and §School of Physics, Trinity College Dublin, Dublin 2, Ireland
‡Thomas Swan & Co. Ltd., Rotary Way, Consett, County Durham DH8 7ND, United Kingdom

Ⓢ *Supporting Information*

ABSTRACT: In order to fulfill their potential for applications, it will be necessary to develop large-scale production methods for two-dimensional (2D) inorganic nanosheets. Here we demonstrate the large-scale shear-exfoliation of molybdenum disulfide nanosheets in aqueous surfactant solution using a kitchen blender. Using standard procedures, we measure how the MoS$_2$ concentration and production rate scale with processing parameters. However, we also use recently developed methods based on optical spectroscopy to simultaneously measure both nanosheet lateral size and thickness, allowing us to also study the dependence of nanosheet dimensions on processing parameters. We found the nanosheet concentration and production rates to depend sensitively on the mixing parameters (the MoS$_2$ concentration, C_i; the mixing time, t; the liquid volume, V; and the rotor speed, N). By optimizing mixing parameters, we achieved concentrations and production rates as high as 0.4 mg/mL and 1.3 mg/min, respectively. Conversely, the nanosheet size and thickness were largely invariant with these parameters. The nanosheet concentration is also extremely sensitive to the surfactant concentration. However, more interestingly the nanosheet lateral size and thickness also varied strongly with the surfactant concentration. This allows the mean nanosheet dimensions to be controlled during shear exfoliation at least in the range ~40−220 nm for length and ~2−12 layers for thickness. We demonstrate the importance of this by showing that the MoS$_2$ nanosheets prepared using different surfactant concentrations, and so displaying different nanosheets sizes, perform differently when used as hydrogen evolution catalysts. We find the nanosheets produced using high surfactant concentrations, which gives smaller flake sizes, perform significantly better, consistent with catalysis occurring at nanosheet edges. Finally, we also demonstrate that shear exfoliation using a kitchen blender is not limited to MoS$_2$ but can also be achieved for boron nitride and tungsten disulfide.
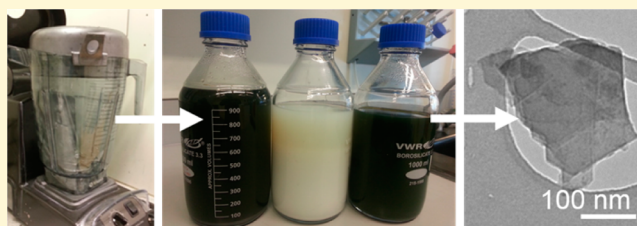
INTRODUCTION

Over the past few years the study of two-dimensional nanomaterials such as graphene[1,2] and molybdenum disulfide (MoS$_2$)[3−5] has become one of the most important areas of materials science. Such materials show potential in a range of applications from electronics to electrochemistry. Perhaps the most versatile way of making two-dimensional nanosheets is by liquid phase exfoliation of layered crystals.[6−9] In this method, layered crystallites are ultrasonicated in certain stabilizing liquids such as appropriate solvents[8,10,11] or solutions of surfactants[12−14] or polymers.[15,16] This results in the production of nanosheets which are stabilized against aggregation via the interaction with the liquid.[12,15,17,18] This method has been used to successfully produce dispersions of nanosheets of a range of materials, including graphene,[8,19] BN,[6,20] and various transition metal dichalcogenides[6,10,21,22] such as MoS$_2$ and WSe$_2$. Using sonication-assisted exfoliation, dispersions of volumes typically in the range of hundreds of milliliters can be produced.[23] The nanosheets are typically a few layers thick and of lateral sizes in the range ~50 nm to 2 μm, depending on the material. Importantly these nanosheets tend to be free of basal plane

defects.[8,23] Such dispersions can be used to process the nanosheets into functional structures such as films, networks, and composites.[20,24−26] Such structures have proven useful in a range of application areas including plasmonics,[27] photodetectors,[24,28,29] electrodes in dye-sensitized solar cells,[30] supercapacitors[31] and batteries[26,32] or electrocatalysts[33] for hydrogen evolution.

More recently it has been demonstrated that liquid exfoliation can be achieved by exposing graphite to high shear rates[34] using either rotor-stator high shear mixers[35,36] or simple kitchen blenders.[37,38] This gives graphene nanosheets of similar size and quality to those produced using sonication. The advantage of this technique is that much higher volumes can be produced compared to sonication, and so much higher production rates can be achieved. Such work has allowed liquid phase exfoliation of graphite to be scaled up toward an industrial process for graphene production. However, to date

only preliminary results have been demonstrated for the scale-up of liquid phase exfoliation of inorganic layered materials such as MoS_2, WS_2, and BN.[34,35] To facilitate scaleup, it will be important to demonstrate an effective large-scale shear exfoliation of such materials with rotating blade mixers and to identify optimized processing parameters.

In addition, liquid phase exfoliation tends to produce nanosheets with a very broad size distribution. In the case of graphene it would not be unusual for the lateral nanosheets size in a given batch to vary from 100 nm to 2 μm.[39,40] This is a problem because many applications require specific nanosheets sizes. For example, composite reinforcement requires large nanosheets[16] at least ~2 μm in length, while catalysis of hydrogen production requires small nanosheets with length below 100 nm.[41] This problem has previously been addressed by size selection.[39,40] In the simplest case, this can be achieved by controlled centrifugation: low centrifugation rates remove large nanosheets, while high centrifugation rates separate out smaller nanosheets. However, while this works well, it is nevertheless an additional postprocessing step. It would be much better, and more time and energy efficient, to control the nanosheet size during the exfoliation step.

In this work we simultaneously resolve both of these problems. We demonstrate that molybdenum disulfide can be exfoliated in aqueous surfactant solutions under shear at the liter scale using a kitchen blender. We characterize how the processing parameters affect the concentration, length, and thickness of the nanosheets. We find that all processing parameters influence the concentration and so the production rate. However, we find the nanosheet's length and thickness to be relatively invariant with all production parameters except the surfactant concentration. We find the surfactant concentration to strongly influence the nanosheet length and thickness. By adjusting the surfactant concentration, we can controllably vary the nanosheets length between ~40 and ~200 nm and the thickness between ~2 and ~12 layers. We quantify the scaling of nanosheets concentration with all processing parameters allowing us to identify an optimized parameters set, leading to concentrations as high as 0.5 mg/mL, nanosheet yields approaching 1%, and production rates of ~1 mg/min. We show that this methodology can be applied not only to MoS_2 but also to WS_2 and BN. Finally we demonstrate the importance of size control by producing hydrogen evolution reaction (HER) catalysts from different sizes of nanosheets: we find the hydrogen production rate to increase with decrease in nanosheets size as expected.

■ RESULTS AND DISCUSSION

Initial Trials. In this work we study the exfoliation of bulk MoS_2 layered crystals to give MoS_2 nanosheets using a Vitamix XL Variable Speed blender (Figure 1A). This blender consists of a tapered jug, ~150 mm diameter at the base, expanding to ~220 mm at the top with a capacity of 5.5 L (though working volume is only ~2 L due to problems associated with foaming). It is fitted with four baffles which are designed to suppress rotation of the liquid as a whole and so increase turbulence. These are fixed to the walls, projecting ~9 mm into the jug, with a width of ~2 mm and extend the full height of the jug. The impeller is shown in Figure 1B and consists of 4 blades with a diameter of ~110 mm. Two are angled slightly above horizontal, while two are angled below horizontal (Figure 1B). It is fitted with a 1900 W motor with variable speed control. We measured the maximum rotation rate to be 8335 rpm and
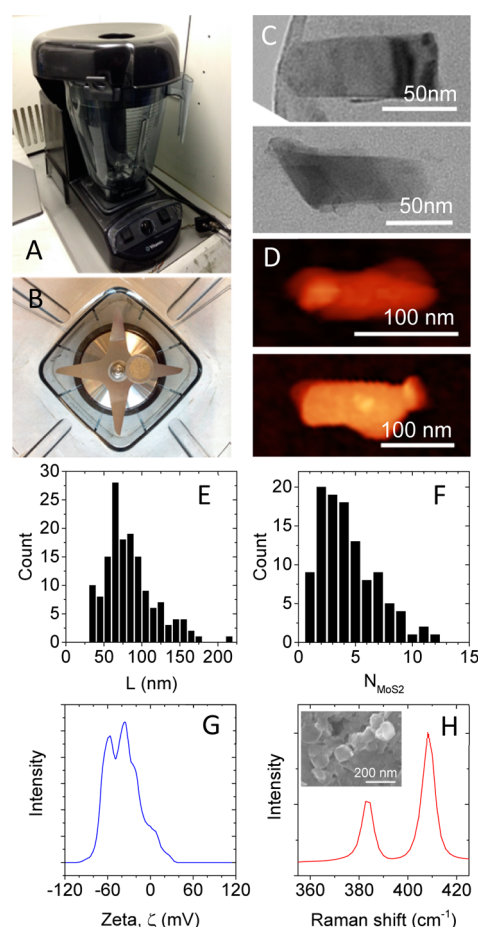

Figure 1. A) Photograph of the Vitamix blender used in this study. B) The blade is shown with a €2 coin for comparison. C−D) TEM and AFM images of typical flakes produced using standard mixing parameters (see below). E−F) Histograms showing flake size statistics for E) flake length measured by TEM and F) flake thickness measured by AFM (expressed as number of monolayers per flakes, N_{MoS2}) measured on flakes produced using standard processing parameters. G) Zeta potential distribution plot of a dispersion of MoS_2 nanosheets produced using parameters below. H) Raman spectrum collected from a vacuum-filtered film of MoS_2 nanosheets. Inset: SEM image of the surface of such a film. All data in this figure was measured on nanosheets produced using standard conditions: C_i = 50 mg/mL, C_{surf} = 10 mg/mL, t = 120 min, N = 8335 rpm, V = 1000 mL.

developed an accurate speed control and measurement system (see the SI). Because the blender is predominately made from plastic, we decided to attempt to exfoliate MoS_2 in an aqueous surfactant solution. Surfactant exfoliation of layered materials such as graphene and MoS_2 has been extensively studied over the past few years.[13,42−44] We chose sodium cholate as the surfactant as this is commonly used to stabilize liquid-exfoliated layered materials.[13]

In a typical experiment, the required mass of powdered MoS_2 was added to the jug and an aqueous surfactant solution with a known concentration poured in on top. In addition to the MoS_2 concentration, C_i, and surfactant concentration, C_{surf}, the parameters that can be controlled during a mix are the mixing time, t, the liquid volume, V, and the rotor speed, N. Also, we note that the rotor diameter generally affects the mixing outcome, but this is of course fixed here. After preliminary trials, we chose a set of standard parameters for mixing: C_i = 50 mg/mL, C_{surf} = 10 mg/mL, t = 120 min, N = 8335 rpm (full

speed), V = 1000 mL. Mixing under these conditions yields a dark colored liquid. This was centrifuged using a Hettich Mikro 220R centrifuge at 1,500 rpm (240 g) for 90 min to remove any unexfoliated material. The top 50% of the supernatant was then collected for analysis.

To ascertain the nature of the dispersed material, we performed transmission electron microscopy (TEM) analysis, with typical images shown in Figure 1C. These images clearly show planar objects with length of ∼100 nm and width roughly half that and are consistent with what is usually observed for exfoliated layered compounds.[6,22,39] To further analyze these objects, a few drops of supernatant were deposited onto Si/SiO₂ and analyzed by atomic force microscopy (AFM). Shown in Figure 1D are two representative AFM images of the deposited objects. We note that they are very similar in appearance to the nanosheets imaged in TEM. We measured the longest dimension (the length, L) of ∼100 objects observed in the TEM with the data presented in Figure 1E as a histogram. We found a mean length of ∼85 nm, very similar to that found by analysis of the AFM data (∼95 nm) and consistent with the size of exfoliated MoS₂ nanosheets produced by sonication and centrifugation under similar conditions.[39] The AFM length is typically overestimated compared to TEM due to broadening effects from cantilever-substrate and sample interactions. However, the comparable size determined by AFM and TEM strongly suggests that aggregation phenomena during deposition were minimal. One of the advantages of AFM over TEM is that it can give nanosheet thickness information once care is taken to calibrate the data[35,39] (see Methods). Shown in Figure 1F is AFM thickness data presented as the number of monolayers per nanosheet, N_{MoS_2}. This data shows the nanosheets to be predominately thinner than 10 layers with a mean thickness of N_{MoS_2} = 4.6. This is reasonably thin and comparable to MoS₂ nanosheets produced by sonication which have thicknesses between 1 and 10 layers.[39] For further comparison, shear-exfoliated graphene nanosheets have a mean thickness of ∼6 layers.[35]

Colloidal particles that are coated by surfactant are stabilized by repulsive interparticle interactions.[18,45] Such repulsions are due to the combination of an adsorbed layer of ionized tail groups and a diffuse cloud of counterions: the electrical double layer. The double layer results in a repulsive electric field which prevents aggregation of nearby particles. We can characterize this repulsion via the zeta potential[18,45] of the surfactant-coated nanosheets.[12,44] Shown in Figure 1G is the measured zeta distribution plot for a nanosheet dispersion prepared using the standard exfoliation conditions mentioned above. The zeta distribution is relatively broad extending from close to zero to −80 mV and appears to be multimodal. This is in contrast to graphene in SC[44] or chemically exfoliated MoS₂,[46] where distributions are typically monomodal and somewhat narrower.

It is very important to confirm that the surfactant-stabilized nanosheets observed in the dispersion are actually MoS₂. To do this, we vacuum filtered a portion of the dispersion to produce a thin film on a porous membrane. SEM imaging showed the resultant film to consist of a disordered array of 2D nanosheets (inset Figure 1H). To confirm the nature of these nanosheets, we performed Raman spectroscopy on the films. Shown in Figure 1H is a typical Raman spectrum excited at 532 nm showing the characteristic E₂g (382 cm⁻¹) and A₁g phonons (408 cm⁻¹) of MoS₂.[47] No pronounced peak shifts compared

to bulk MoS₂ crystals are observed. This is because (i) a film of randomly restacked nanosheets is measured and (ii) the majority of nanosheets are few-layered where no shifts in phonon energies are expected.[48,49] However, Raman spectroscopy is important, as it also shows that no vibrations other than Mo−S are observed (e.g., no oxides are detected).

We can further confirm the nature of the dispersed nanosheets using optical extinction spectroscopy. (N.B. this technique is usually referred to as absorption spectroscopy. However, because the optical beam interacts with the dispersed nanosheets by both absorption and scattering, extinction spectroscopy is a more appropriate term.[39,50]) Shown in Figure 2A are optical extinction spectra (normalized by cell length, i.e.
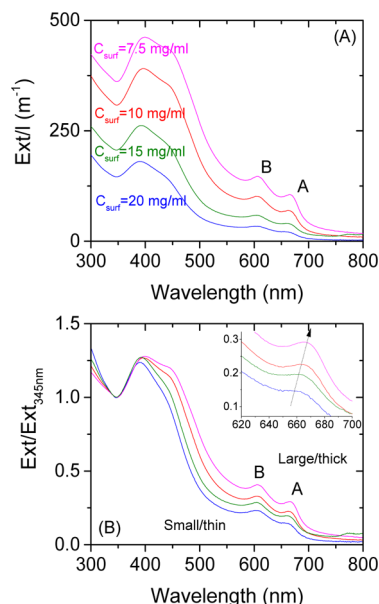

Figure 2. A) Extinction spectra for dispersions of shear exfoliated MoS₂ produced with a single concentration of MoS₂ powder (C_i = 30 mg/mL) but a range of surfactant concentrations (C_{surf}). B) The same spectra normalized to the local minimum at 345 nm. It is clear that both the intensity at the B-exciton (Ext_B/Ext_{345}) and the position of the A-exciton (λ_A, see inset) vary with C_i. This indicates that both nanosheet length and thickness vary with C_i. Mixing conditions were t = 120 min, N = 8335 rpm, V = 1000 mL.

Ext/l), for a number of dispersions prepared with different surfactant concentrations (see the caption for details). These spectra are clearly consistent with MoS₂ nanosheets, displaying A- and B-excitonic transitions as well as the other features consistent with the 2H polytype of MoS₂.[39,51]

Measuring Concentration, Length, and Thickness. However, apart from confirming the nature of the dispersed phase, such spectra contain additional information. At the most basic, because the extinction coefficient of dispersed MoS₂ nanosheets is known to be 6,820 L g⁻¹ m⁻¹ at the local minimum at 345 nm,[39] such spectra can be used to measure the dispersed nanosheet concentration. Below, we will use this to measure the MoS₂ concentration as a function of mixing parameters, in a manner similar to that recently reported for shear-exfoliated graphene.[35,37]

However, in addition to concentration information, it has recently been shown that the extinction spectrum of MoS₂ nanosheets carries information about both the mean nanosheet length and thickness.[39] The length effects are due to the effect

of nanosheet edges on the spectral profile, while quantum confinement effects result in well-defined shifts in A-exciton position with nanosheet thickness. As a result, the length can be determined from the ratio of extinction at the B-exciton to that at 345 nm, (Ext_B/Ext_{345}):

$$L\ (\mu m) = \frac{3.5 Ext_B/Ext_{345} - 0.14}{11.5 - Ext_B/Ext_{345}} \quad (1a)$$

while the nanosheet thickness (expressed as number of monolayers per nanosheet) can be determined from the wavelength associated with the A-exciton, λ_A:

$$N_{MoS_2} = 2.3 \times 10^{36} e^{-54888/\lambda_A} \quad (1b)$$

This is extremely useful as it allows us to investigate not only the dependence of concentration but also the dependence of nanosheet dimensions on processing parameters. In the past, such a study would have required large amounts of AFM/TEM analysis and would have been prohibitively time-consuming.

The presence of such effects can clearly be seen in Figure 2B which shows the same spectra as in Figure 2A but normalized to the extinction at 345 nm. Clearly, both (Ext_B/Ext_{345}) and λ_A vary with surfactant concentration, showing the nanosheet dimensions to be sensitive to the amount of surfactant present. This will be discussed in more detail below.

The Effect of Surfactant Concentration. The aim of this study is both to begin scale-up of MoS_2 exfoliation and to understand the effect of processing parameters on nanosheet concentration, length, and thickness. However, first it is necessary to characterize the effect of surfactant concentration and so optimize the amount of surfactant required. It is important to do this first as nanosheet dispersions can be very sensitive to surfactant content, perhaps more so than any other parameter.[37] To do this, we prepared a number of MoS_2 dispersions, varying the surfactant concentrations in different ways. Specifically, the MoS_2 concentration was fixed at values of C_i = 50, 30, and 10 mg/mL and in each case a set of dispersions prepared with a range of surfactant concentrations. Two additional sets of dispersions were prepared, each varying C_{surf} but with fixed ratios of C_{surf}/C_i of 0.4 and 0.2. In all cases, the extinction spectra were measured, and the MoS_2 concentration, C, nanosheet length, L, and thickness, N_{MoS_2}, were calculated.

Shown in Figure 3A are data for the yield, Y (defined as $Y = (C/C_i)$) of MoS_2 nanosheets plotted as a function of C_{surf}. This graph is remarkable as it is clear that all data points fall onto the same master curve, demonstrating that the nanosheet yield is controlled by C_{surf}. As the surfactant concentration is increased, the yield increases until C_{surf} = 5–10 mg/mL, where it saturates before falling off at higher values of C_{surf}. We found that empirically, such behavior is described by $Y = [14C_{surf}^{-0.8} + 0.14C_{surf}^{1.4}]^{-1}$, an observation which will come in useful later on (see dashed line on Figure 3A). We note that this behavior is distinct to that observed for graphene produced by shear-exfoliation in a slightly different blender with a different surfactant, where we found the graphene concentration to depend on the ratio of C_{surf}/C_i rather than C_{surf} alone.[37]

Shown in Figure 3B and C are data for the mean nanosheet length, L, and thickness, N_{MoS_2}, as a function of C_{surf}. In both cases, the same behavior is observed with all data falling on the master curves. Again, this is an important result as it shows both L and N_{MoS_2} to be controlled solely by C_{surf}. The C_{surf} dependence of both L and N_{MoS_2} are similar: both initially
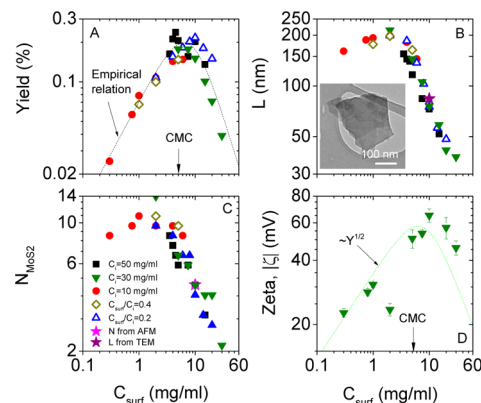
Figure 3. Characterization of optimum surfactant content. A) MoS_2 nanosheet yield (defined as $Y = C/C_i$) plotted versus surfactant concentration, C_{surf}, for five sets of samples (see the caption in C). The dashed line shows the empirical relation described in the text. B–C) Nanosheet dimensions as calculated from the optical extinction spectra using eqs 1a and 1b. B) Length, L, and C) thickness, N_{MoS_2} (expressed as number of monolayers per nanosheet) plotted versus C_{surf} for five sets of samples. Also shown in B) and C) is the mean nanosheet thickness as measured by AFM and length as measured by TEM. The inset in B) shows a TEM image of a relatively large MoS_2 nanosheet, prepared C_i = 10 mg/mL and C_{surf} = 2 mg/mL. D) Zeta potential (expressed as $|\zeta|$) as a function of C_{surf}, for the samples with C_i = 30 mg/mL. The dashed line represents the square root of the empirical relation in A, rescaled to overlay the data. This agreement is consistent with the MoS_2 concentration scaling with ζ^2. All samples in this figure were prepared with t = 120 min, V = 1 L, and N = 8,335 rpm.

increase slightly with C_{surf} before peaking around C_{surf} = 2 mg/mL and falling off at higher surfactant contents. For $C_{surf} \sim 2$ mg/mL, the nanosheets are relatively large[39] with lateral sizes of 200–250 nm (see inset for TEM image). However, they are also quite thick, displaying values of $N_{MoS_2} \sim 10$. Conversely, at higher values of $C_{surf} \sim 30$ mg/mL the nanosheets are very thin with values of $N_{MoS_2} \sim 2$. However, they are also very small with $L \sim 40$ nm. This data implies, as observed previously,[39,52] that the nanosheet thickness tends to be correlated with the length. However, the most important aspect of this data is that length and thickness can be controlled by varying a processing parameter, namely C_{surf}. Control of flake dimensions is very important as many applications are size specific. For example, while electrical applications probably require large nanosheets, catalytic applications (see below) require small ones.[41] While nanosheet size can be selected using postexfoliation processing,[39,40] we believe this is the first example of in situ size control.

To attempt to understand the dependence of Y, L, and N_{MoS_2} on C_{surf}, we measured the zeta potential on a subset of samples (those with C_i = 30 mg/mL). All zeta potentials were negative as expected. Plotted in Figure 3D are the mean absolute zeta potentials, i.e $|\zeta|$, as a function of C_{surf}. Interestingly, $|\zeta|$ initially increases until C_{surf} = 5–10 mg/mL before falling off at higher values of C_{surf}, in a manner reminiscent of the yield, Y. Previously,[44] we showed that the concentration of surfactant-stabilized graphene dispersions tends to scale as $C \propto \zeta^2$. If this is true here then, because $Y = (C/C_i)$, we would expect $|\zeta| \propto \sqrt{Y}$. To test this, we plot the square root of the empirical function described above, as a function of C_{surf} in Figure 3D. When appropriately scaled, this function matches the ζ versus C_{surf} data reasonably well confirming that $Y \propto C \propto \zeta^2$.

This allows to propose a tentative model for the behavior observed in Figure 3. Below C_{surf} = 5−10 mg/mL, $|\zeta|$ increases with C_{surf}, consistent with increasing coverage of surfactant molecules per nanosheet. Higher absolute zeta potentials result in larger internanosheet potential barriers and high exfoliation yield. However, the critical micelle concentration (CMC) of sodium cholate is at C_{surf} ∼6 mg/mL. When this surfactant concentration is reached, the concentration of individual surfactant molecules stops increasing and so the surfactant coverage peaks, leading to saturating of $|\zeta|$ and so Y. As C_{surf} is increased further, the micelle concentration grows, increasing the importance of the depletion interaction.[18,45] This destabilizes the surfactant-coated nanosheets leading to a decreased dispersed concentration.

It is more difficult to explain the dependence of length on C_{surf}. However, at very low C_{surf} and therefore low surfactant packing density, it is probable that predominantly small nanosheets are stabilized. We rationalize this because smaller nanosheets are easier to exfoliate, as the net cost of exfoliation is lower due to the lower surface area. Thus, when increasing the surfactant concentration, the population of larger nanosheets slightly increases. However, after full surfactant coverage is reached above the CMC of sodium cholate, the mean length of the nanosheets falls off again. We suggest that this is associated with the fact that the surfactant packing density at edges is probably different compared to that at the center of the nanosheets. This is reasonable from both geometrical aspects and from previous observations[39] that edges of MoS$_2$ nanosheets are electronically distinct from the basal plane potentially leading to a different strength of the interaction of the surfactant and the nanomaterial. The data in Figure 3B suggests that the packing density of SC is higher at edges compared to basal plane MoS$_2$. Thus, as the surfactant concentration is increased beyond the concentration necessary to achieve full coverage, the population of smaller nanosheets increases (as more surfactant is bound to them) and thus L decreases. We reason that this different packing density at edge and center is also responsible for the unusually broad zeta potential distribution plots as mentioned above. However, we accept that this explanation is tentative. A full understanding of the surfactant adsorption is beyond the scope of this manuscript.

The Effect of Mixing Parameters. Once we have characterized the surfactant concentration dependence, we can set C_{surf} at a constant value and systematically explore the effect of mixing parameters on nanosheet concentration, length, and thickness. As described above, the relevant mixing parameters are mixing time, t, liquid volume, V, MoS$_2$ starting concentration, C_i, and blade rotation rate, N. We studied the effect of mixing parameters by fixing C_{surf} = 10 mg/mL and the other parameters at their standard values (see above) and systematically varying one parameter at a time.

Shown in Figure 4A are data for dispersed MoS$_2$ concentration, plotted versus mixing time. As the mixing time is increased from 60 to 600 min, the concentration increases from 0.05 to 0.4 mg/mL. This upper value is much higher than that previously reported for similar studies on high shear mixing of MoS$_2$ and compares well to sonicated MoS$_2$ dispersions.[22] As with blender exfoliation of graphene, the concentration initially scales linearly with time.[35] However, for t > 120 min, the behavior becomes slightly sublinear. Even so, over the whole range, the data is reasonably well described by $C \propto t^{0.88}$. This is in contrast to both sonication-assisted exfoliation[23] and shear
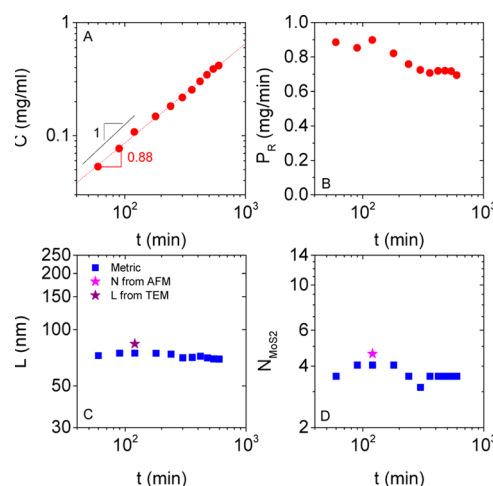

Figure 4. Dependence of dispersion and nanosheet properties on mixing time. A) Dispersed concentration (after centrifugation) plotted versus mixing times for samples prepared with C_i = 50 mg/mL, C_{surf} = 10 mg/mL, N = 8,335 rpm, V = 1,000 mL. The red dashed line illustrates power-law behavior with the exponent of 0.88. The black line represents linearity. B) Same data as in A) but transformed to represent production rate, P_R, using $P_R = (CV/t)$. C−D) Nanosheet length, L, and thickness, N_{MoS_2}, as calculated from the optical extinction spectra using eqs 1a and 1b. Also shown in B) and C) is the mean nanosheet thickness as measured by AFM and length as measured by TEM.

exfoliation in solvents[35] which both show time exponents closer to 0.5. In terms of large scale manufacturing, the production rate, $P_R = (CV/t)$, is more important than the concentration.[35] This rate is shown as a function of time in Figure 4B. In line with the concentration data, P_R is constant at ∼0.9 mg/min for times up to ∼120 min after which it falls off slightly.

While the dependence of both concentration and production rate on mixing time has been reported previously,[35,37] very little is known about the dependence of nanosheet length and thickness on mixing time or indeed any other processing parameter. This is because nanosheet size measurements are usually very time-consuming. However, because of the metrics described above, measurement of nanosheet dimensions is straightforward here. Shown in Figure 4C and D are data for nanosheet length and thickness, respectively, plotted versus mixing time. In both cases, the data is invariant with time, displaying values of L ∼ 70 nm and N_{MoS_2} ∼ 4 layers, respectively. These values are consistent with values measured by TEM and AFM which are also shown. We note that this behavior is very different than that found for sonication-assisted exfoliation of both graphene and MoS$_2$ where the flake size falls with sonication time due to scission effects.[22,23] The behavior observed here is a great advantage because it allows the high concentrations associated with long processing times to be achieved without the cost of reduced nanosheet size.

Shown in Figure 5A and B respectively are data for concentration and production rate of MoS$_2$ nanosheets as a function of liquid volume, V. The concentration falls off with volume as $C \propto V^{-0.41}$. Such power law behavior has been observed previously for graphene produced in both high shear mixers[35] and kitchen blenders[37] where exponents of −0.68 and −0.16 were observed, respectively. These large and small exponents were, respectively, were suggested to be associated with the localized and delocalized nature of the exfoliation
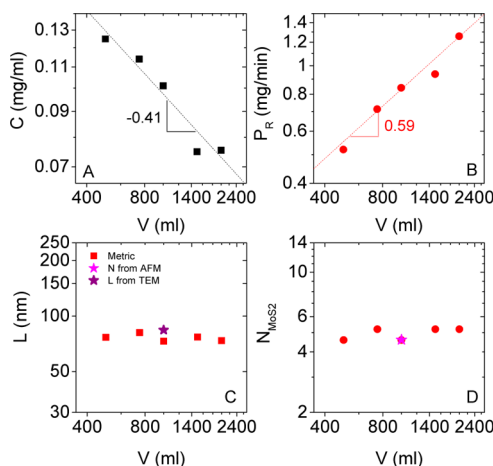
Figure 5. Dependence of dispersion and nanosheet properties on liquid volume. A) Dispersed concentration (after centrifugation) plotted versus liquid volume (C_i = 50 mg/mL, C_{surf} = 10 mg/mL, t = 120 min, N = 8,335 rpm). The dashed line illustrates power-law behavior with an negative exponent of 0.41. B) Same data as in A) but transformed to represent production rate, P_R, using $P_R = (CV/t)$. The dashed line illustrates power-law behavior with an exponent of 0.59. C−D) Nanosheet length and thickness as calculated from the from the optical extinction spectra using eqs 1a and 1b. Also shown in C) and D) is the mean nanosheet thickness as measured by AFM and length as measured by TEM.

volume in the high-shear mixer and blender. In a high shear mixer, the high shear rates required for exfoliation only occur in a small volume in the vicinity of the mixing head, leading to a large negative volume exponent−as the volume increases a smaller and smaller fraction of liquid is near the mixing head. Conversely, in the previous blender study,[37] high turbulent shear rates were produced throughout the vessel, leading to a low negative volume exponent (as exfoliation is occurring everywhere, increasing the volume does not have a significant negative impact on nanosheet production). As we would expect the exfoliation volume in the blender used here to be delocalized, it is somewhat surprising that the exponent is not smaller than observed. However, it is worth noting that, for the blender used here, N = 8,335 rpm, leading to a volume exponent of −0.41. This can be compared the previous study on graphene exfoliation which used a blender with N = 18,000 rpm, leading an exponent of −0.16. It is possible that the lower rpm used here cannot generate high enough local turbulent shear rates throughout the jug resulting in a partial localization of exfoliation volume and a correspondingly larger negative volume exponent. The production rate is of course related to the concentration by $P_R = (CV/t)$ in meaning P_R increases as $V^{0.59}$, reaching 1.3 mg/min at a volume of 2 L (Figure 5B).

Both nanosheet length and thickness are shown as a function of volume in Figure 5 C and D with the equivalent TEM/AFM data included to verify the accuracy of the metric data. In both cases, the data is invariant with volume, with values of $L \sim 70-80$ nm and $N_{MoS_2} \sim 5$ layers, respectively. This invariance with volume has practical importance because it means large scale production at high volume can be achieved without sacrificing nanosheet lateral size and thickness

The remaining two processing parameters, C_i and N, are slightly different than those discussed above, as each can only influence the production rate via the exfoliated MoS_2 concentration (i.e., because $P_R = (CV/t)$) in contrast to V

and t which directly affect the production rate. Thus, in Figure 6A, we show data for exfoliated MoS_2 concentration, but not
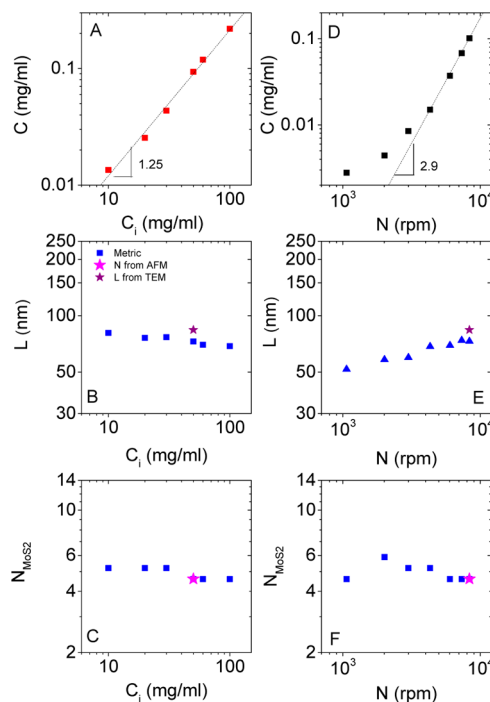

Figure 6. Dependence of dispersion and nanosheet properties on starting concentration of MoS_2 powder, C_i, and rotor speed, N. A and D) Dispersed concentration (after centrifugation) plotted versus A) C_i and D) N (C_i = 50 mg/mL, C_{surf} = 10 mg/mL, t = 120 min, N = 8,335 rpm, V = 1,000 mL). The dashed line illustrates power-law behavior with the exponents shown in the panels. B and E) Nanosheet length and thickness as calculated from the optical extinction spectra using eqs 1a and 1b. Also shown in C and F) is the mean nanosheet thickness as measured by AFM and length as measured by TEM.

P_R, versus the initial MoS_2 powder concentration (i.e., mass of powder added to jug/liquid volume). We observe a steady increase in C with increasing C_i, reaching C = 0.22 mg/mL for C_i = 100 mg/mL. However, it is important to note that C increases superlinearly with C_i, consistent with $C \propto C_i^{1.25}$. This result is reproducible and is in contrast with our studies on shear exfoliation of graphene which have always shown $C \propto C_i$.[35,37] Interestingly the nanosheets get slightly smaller and thinner (Figure 6 B and C) as C_i is increased from 10 to 100 mg/mL, for example falling in length from 81 to 69 nm.

In order to control the rotor speed, N, the blender had to be somewhat modified as described in the SI. The exfoliated MoS_2 concentration is plotted versus N in Figure 6D and shows a steady increase in C with N, reaching C = 0.1 mg/mL for N = 8,335 rpm. The data shows an initial slow increase of C with N before a rapid rise which occurs at an onset value of $N_c \sim 4,000$ rpm. Above this onset, the concentration increases with N as $C \propto N^{2.9}$.

This sort of behavior has been observed for graphene exfoliated in both high-shear mixers and blenders.[35,37] However, significant differences exist. For graphene, in these mixers/blenders, the minimum rpm was significantly lower, $\sim 1,000$ and $\sim 1,800$ rpm, respectively. The value of N_c = 1,800 rpm observed for graphene production in a kitchen blender is most comparable to the situation here.[37] It is known that for exfoliation to occur, the layered material must experience shear

rates above some critical value, $\dot{\gamma}_c$, which was measured to be 10^4 s^{-1} for graphene exfoliation. Previously,[37] we suggested that, in blenders, the exfoliation first occurs when the rotating blade begins to deposit enough power into the liquid such that the turbulent shear rates begin to exceed the minimum shear rate in appreciable volumes of the blender. This allowed us to express the critical rotor speed for exfoliation as

$$N_c = \left[\frac{\eta V \dot{\gamma}_c^2}{k_1 k_2 \rho N_p D^5}\right]^{1/3} \quad (2)$$

where η, ρ, and V are the liquid viscosity, density, and volume, and $\dot{\gamma}_c$ is the critical shear rate for exfoliation. The parameters N_p and k_2 relate to the blade (and mixing environment): N_p is the power number,[53,54] a constant which relates the energy dissipation rate to rotor speed and diameter, while k_2 is the fraction of inputted power which is dissipated as turbulence (rather than periodic large scale rotational motion). The parameter k_1 is a measure of the distribution of local turbulent energy dissipation rates. Generally, when exfoliation starts to occur, i.e. when $N = N_c$, the mean energy dissipation rate is not high enough to result in a mean turbulent shear rate which is high enough to give exfoliation. However, there is a distribution of local turbulent energy dissipation rates and so a distribution of local turbulent shear rates. Therefore, the onset of exfoliation occurs when high enough local turbulent shear rates exist in an appreciable volume of the jug. The ratio of local energy dissipation rate, when exfoliation can first occur, to mean energy dissipation rate is k_1.

We can compare the results found here ($N_c \sim 4,000$ rpm) to those found previously for blender exfoliated graphene ($N_c \sim 1,800$ rpm), albeit in a different blender.[37] In both cases, the liquid was water meaning η and ρ were the same in both cases. As k_1 is determined by fluid dynamics, it is likely to be invariant between blenders. The main difference was that in previous graphene exfoliation experiments, $V = 300$ mL, while here it was 1,000 mL. Most significantly, the rotor diameter used previously[37] for graphene exfoliation was $D = 55$ mm, while here it was $D = 110$ mm. With this in mind, we can work out that the ratio ($\dot{\gamma}_c^2/k_2 N_p$) is ~ 75 times higher for shear exfoliation of MoS$_2$ in this blender compared to shear exfoliation of graphene in a different blender as described previously. This is almost certainly a combination of $\dot{\gamma}_c$ being higher for MoS$_2$ than for graphene (in the given surfactant environments) and $k_2 N_p$ being lower in the blender currently under study. This result is important for two reasons. First, it highlights the fact that relatively little is known about how $\dot{\gamma}_c$ varies between different layered materials with different initial sizes. This parameter is a direct measure of the strength of the various intermolecular interactions in the system i.e. liquid–liquid, liquid–nanosheet, and nanosheet–nanosheet.[35] Future work will involve measuring $\dot{\gamma}_c$ for a range of layered materials. We suggest that this should be carried out in an environment such as a rheological cell (i.e., a Couette[35]) where the shear rate can be carefully controlled. Second, it illustrates that all blenders are not equal and care must be taken with blade design/suitable mixing vessel/baffles to maximize exfoliation efficiency.

The second main difference to previous work is that the N-exponent of 2.9 measured above is much higher than the values of 1.13 and 0.53 for high shear mixers and blenders, respectively. Why such a difference should be observed is not at all clear. However, it is a useful result from a scale-up

standpoint, as it means large increases in concentration and so production rate can be achieved by increasing N.

Shown in Figure 6E and F are data for the length and thickness of nanosheets as a function of N with TEM/AFM data for verification purposes. The nanosheet length clearly increases from 50 to 74 nm as N is increased from 1,000 to 8,335 rpm. This is the opposite behavior to that observed in rotor-stator mixers and in direct contravention with the simple model outlined by Paton et al. (this predicts that the minimum nanosheet length produced by shear exfoliation scales with $1/N$ and agrees well with experimental data).[35] This behavior is almost certainly a manifestation of small graphite platelets being exfoliated most easily at low rpm. Interestingly, the thickness data shows no clear dependence on N.

Scaling Factor and Overall Behavior. The work described in the previous section allowed us to identify how the dispersed nanosheet concentration depends on the processing parameters C_{surf}, C_i, t, N, and V. Putting together the empirical scaling trends described above gives the following scaling relation

$$C \propto \left[\frac{C_i^{1.25} N^{2.9} V^{-0.41} t^{0.88}}{14 C_{surf}^{-0.8} + 0.14 C_{surf}^{1.4}}\right] \quad (3)$$

where we refer to the term in square brackets as the scaling factor, SF, for short. To test this, we plot C versus SF in Figure 7A for all concentration data shown in Figures 3−6. The data extracted from Figure 3, where C_{surf} was varied, is plotted as blue filled symbols, while the data extracted from Figures 4−6, where C_{surf} was kept constant, but the mixing parameters varied systematically, is plotted as open red symbols. It is clear from this that very good linearity is found right up to the maximum observed concentration of 0.4 mg/mL. To confirm the universality of eq 3 as a scaling law, we prepared six new samples, all with $C_{surf} = 10$ but with randomly chosen values of t, N, C_i, and V. The concentrations were measured and are plotted as the open black symbols. With the exception of the highest SF data point, these data sit on the master curve confirming that eq 3 performs well as a scaling law for nanosheet concentration. From this plot we can extract the proportionality constant in eq 3 to be 6×10^{-14} (when all parameters are expressed as SI units). This allows the expected concentration to be estimated for any combination of processing parameters for example when pilot scale experiments are done with hundreds of liters of MoS$_2$/water/surfactant dispersions.

Another important parameter in liquid exfoliation is the yield, defined above as $Y = (C/C_i)$. We have calculated the yield for all data points in Figure 7A, plotting versus (SF/C_i) in Figure 7B. In the vast majority of cases we find the data to fall on a master curve with very good linearity. This curve shows the measured yield to vary over 2 orders of magnitude with a maximum value of $Y = 0.8\%$. This compares well with the highest yields of 1% we have observed for blender exfoliation of graphene.

However, in terms of scale-up, the most important processing parameter is the production rate ($P_R = (CV/t)$). As with the yield, we have calculated P_R for all the data in Figure 7A. This is plotted versus $V \times (SF/t)$ in Figure 7C. As with C and Y, all data fall well onto a linear master curve. The highest P_R observed was 1 mg/min. This contrasts to blender-exfoliation of graphene which displayed maximum production
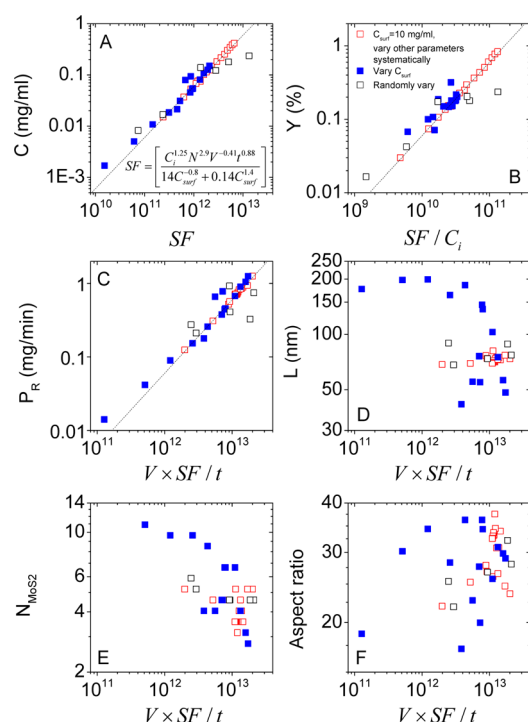
Figure 7. A) Concentration plotted versus scaling factor, *SF*, described in the text and given in the panel. B) Yield ($Y = C/C_i$) plotted versus SF/C_i. C) Production rate ($P_R = CV/t$) plotted *versus* $V \times (SF/t)$. D–F) Length (D), thickness (E), and aspect ratio (F) plotted *versus* $V \times (SF/t)$. In A, B, and C, the dashed lines represents linearity, consistent with $C = 6 \times 10^{-14}$ *SF* (all in SI units). Scaling factor is calculated taking all parameters in SI units. The data is divided into groups where (red) C_{surf} was set at 10 mg/mL, while all other parameters were varied systematically; (black) C_{surf} was set at 10 mg/mL, while all other parameters were varied randomly; and (blue) t, V, and N were fixed, while C_{surf} was varied systematically.

rates of ~3.3 mg/min (though surfactant and processing parameters were different).

One significant advantage of this work over other studies which have examined the production of nanosheets is that we can monitor the length and thickness for every sample. This allows us to look for any trade-offs between production rate and nanosheet size. To facilitate this, we plot both nanosheet length and thickness in Figure 7D and E as a function of $V \times (SF/t)$. This allows us to compare P_R, L, and N_{MoS_2} for any combination of processing parameters and gives an overview of the size measurements performed in this study. In fact, the data for both L and N_{MoS_2} *versus* $V \times (SF/t)$ are both similar in form. For the data sets with constant C_{surf} (open symbols), both L and N_{MoS_2} are reasonably invariant with $V \times (SF/t)$. However, as highlighted above, both the nanosheet length and thickness are strongly dependent on C_{surf} and so $V \times (SF/t)$. This manifests itself as both L and N_{MoS_2} falling by factors of ~4−5 as $V \times (SF/t)$ is increased from 10^{12}−3×10^{13}. However, the size *versus* $V \times (SF/t)$ behavior is only strictly relevant for the data measured here and, unlike the data in Figure 7A−C, is not a general trend. In practice, one could chose C_{surf} in order to tailor the nanosheet size as required and then identify a combination of the four mixing parameters which would give the desired P_R.

The fact that the L and N_{MoS_2} data vary with $V \times (SF/t)$ in the same way suggests the aspect ratio (i.e., length/thickness) is roughly invariant with processing parameters. This is not so unexpected. Previous measurements on both liquid-exfoliated MoS_2 and MoO_3 nanosheets have suggested a linear relationship between nanosheet length and thickness.[39,52] This has been explained by suggesting that in the presence of a fixed energy supply, exfoliation can give large, thick nanosheets or small thin ones. However, because exfoliation energy per nanosheet scales with nanosheet surface area, large, thin nanosheets are energetically expensive. However, the presence of an apparently constant aspect ratio may mask some fluctuations. To test this, we plotted the aspect ratio *versus* $V \times (SF/t)$ in Figure 7F. This graph shows significant variations in aspect ratio with processing parameters. Interestingly, the aspect ratio is highest for high values of $V \times (SF/t)$, where the production rate is maximized.

Other Two-Dimensional Materials. In this work we have shown that it is straightforward to make up to 2 L of liquid-exfoliated, surfactant-stabilized MoS_2 dispersion in a high-powered kitchen blender. Indeed, with a bigger jug considerably larger volumes could be made. Because this process has also been used to produce liquid-exfoliated graphene, it is likely that other layered compounds can be exfoliated in this way. To test this, we applied the same procedure used for MoS_2 to both boron nitride (BN) and WS_2. Shown in Figure 8A is a picture of 1 L dispersions of MoS_2, BN, and WS_2 prepared in this way. To confirm the nature of the dispersed material, Figure 8 B and C show optical extinction spectra for the WS_2 and BN dispersions after three different mixing times. The spectra show typical scaling of concentration with mixing time as observed for MoS_2. In addition, the spectral shapes are typical for the respective materials. While WS_2 has a
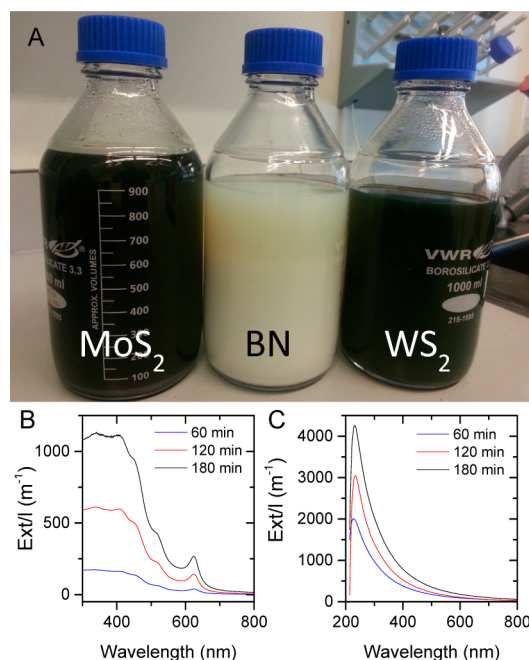

Figure 8. A) Shear exfoliated dispersions of (left to right) MoS_2, BN, and WS_2. B−C) Optical extinction spectra of shear exfoliated dispersions, produced after three different mixing times, of B) WS_2 and C) BN ($C_i = 50$ mg/mL, $C_{surf} = 10$ mg/mL, $N = 8,335$ rpm, $V = 1,000$ mL).

similar spectral profile as MoS_2 with the excitonic transitions clearly discernible,[51] BN shows a featureless extinction spectrum with an onset in the UV region. TEM analysis (SI) shows these dispersions to contain exfoliated nanosheets.

Applications of in Situ Size Control: Hydrogen Evolution Electrocatalysis. The ability to control the nanosheet size during exfoliation, achieved here by control of C_{surf} will be important for a number of applications. It is well-known that MoS_2 nanosheets have a number of applications in electrochemistry.[26,32,55] One important example is as catalysts for the evolution of hydrogen from proton-rich electrolytes.[41,56,57] Because the catalytically active sites reside on the edge of the MoS_2 nanosheet,[41] hydrogen evolution catalysis is strongly dependent on nanosheet length with small flakes performing much better than larger ones. In previous work, nanosheet size has been controlled by a postexfoliation size-selection procedure, with hydrogen production increasing with decreasing nanosheet length. However, it would obviously be better to produce the desired small nanosheets directly in the process. The results described above allow us to do just that.

We prepared three dispersions in the mixer using standard mixing parameters except for the surfactant concentration for which we used C_{surf} = 5, 10, and 20 mg/mL. The measured extinction spectra were used to determine the mean lateral size of nanosheets in these dispersions to be ∼146, ∼100, and ∼75 nm, respectively (nanosheet thicknesses were ∼7.3, ∼5.4, and ∼3.7 layers respectively). Vacuum filtration was used to produce thin films which were transferred onto pyrolytic carbon coated Si/SiO_2 substrates and characterized for hydrogen evolution catalysis (film thicknesses 650−700 nm, see Methods for more information). The current density versus potential curves are shown in Figure 9A with the low current region magnified in the inset. A clear size effect is seen with considerably larger currents and lower onset potentials for the smaller flakes compared with larger ones. Tafel plots of overpotential versus current density (Figure 9B) show the

expected behavior in the low current regime with Tafel slops between 115 and 164 mV/decade. We can see the size dependence more clearly by plotting the current density at a fixed potential (0.4 V) versus flake length in Figure 9C. By increasing the surfactant concentration from 5 to 20 mg/mL and so decreasing nanosheet lateral size from 146 to 75 nm, the current density can be increased from 1.5 to 6.5 mA/cm². Alternatively, we can look at the size dependence of the onset potential (i.e., the potential where J = 1 mA/cm²). In the same size range, this decreases from 0.38 to 0.27 V. This data clearly shows the advantages associated with the ability to control nanosheet size during the nanosheet production procedure. In addition, we found these MoS_2 electrodes to be very stable as described in the SI.

CONCLUSIONS

In this work we have demonstrated liquid phase exfoliation of molybdenum disulfide in aqueous surfactant solution at the liter scale using a commercial kitchen blender. By analyzing the optical extinction spectra, we have determined how the nanosheet concentration, length, and thickness depend on processing parameters (i.e., the surfactant concentration, C_{surf}, the MoS_2 concentration, C_i, the mixing time, t, the liquid volume, V, and the rotor speed, N). We have found the nanosheet concentration to depend on all of the above processing parameters, allowing us to generate well-defined scaling laws. This enables us to identify optimized processing parameters leading to concentrations as high as ∼0.5 mg/mL, nanosheet yields approaching 1%, and production rates of ∼1 mg/min. However, the nanosheet length and thickness were generally invariant with all processing parameters except the surfactant concentration. By varying surfactant concentration, both length and thickness could be controlled over a significant range, allowing in situ size control for the first time. We demonstrate the importance of size control by using these nanosheets as electrocatalysts for hydrogen production. As expected, smaller nanosheets gave the highest rates of hydrogen production. Furthermore, we showed a large-scale shear exfoliation is not only confined to molybdenum disulfide but also can be achieved for WS_2 and BN. We anticipate that these approaches can be applied to the exfoliation of a wide range of layered compounds.

METHODS

Experimental Section. *Materials.* MoS_2 powder (69860, ∼6 μm (max. 40 μm)), WS_2 (243639, 2 μm, 99%), BN (255475, ∼1 μm, 98%), and sodium cholate hydrate (≥99%, C1254) were purchased from Sigma-Aldrich at the highest available purity and used as received. We used deionized water throughout this shear exfoliation study.

Shear Exfoliation. The required mass of MoS_2 powder was weighed and added to the jug. Sodium cholate hydrate was dissolved in a predetermined volume of deionized water by stirring and poured onto the jug on top of the MoS_2 powder. This mixture was then mixed by the rotating blade for a set time. To avoid overheating of both motor and liquid, we applied a duty cycle of 3 min on/3 min off. For each chosen mixing time, 10 mL aliquots were collected and centrifuged (Hettich Mikro 220R, fixed angle rotor) at 1,500 rpm (240 g) for 90 min to remove unexfoliated MoS_2. The top 50% was decanted and retained for analysis, while the sediment was discarded.

Characterization. Optical extinction was measured on a Varian Cary 50 UV−vis spectrophotometer in quartz cuvettes with a path length of 1 cm. The dispersions were diluted by aqueous surfactant solution with equal surfactant concentrations immediately prior to the measurement to yield optical densities below 1.5.
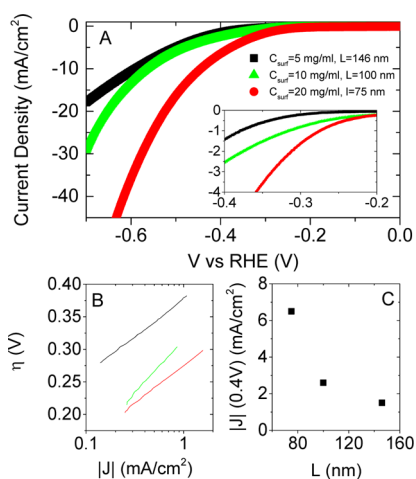

Figure 9. A) Linear sweep voltammograms (5 mV/s) for films MoS_2 on pyrolytic carbon substrates, comparing the electrocatalytic response toward hydrogen evolution reaction. The MoS_2 was prepared using three different surfactant concentrations so the three samples consisting of nanosheets with different mean lengths (see legend). Measured potentials were subjected to iR correction, while the supporting electrolyte was 0.5 M H_2SO_4. Inset: The low current regime. B) Tafel plots for each MoS_2 film. The color coding is as in A. C) Current density produced at 0.4 V plotted versus nanosheet size.

Zeta potential measurements were carried out on a Malvern Zetasizer Nano system with irradiation from a 633 nm He−Ne laser. The samples were injected in folded capillary cells, and the electrophoretic mobility (μ) was measured using laser Doppler velocimetry. The electrophoretic mobility relates the drift velocity of a colloid (ν) to the applied electric field (E); $\nu = \mu E$. All measurements were conducted at 20 °C. The zeta potential ζ is related to the measured electrophoretic mobility μ according to the Smoluchowski approximation. The mean of 5 measurements is reported. Due to the broad and multimodal distribution, we extracted the maximum observed value of zeta for the plot in Figure 3. In the majority of cases, this was also the main component in the distribution.

Bright field transmission electron microscopy imaging was performed using a JEOL 2100, operated at 100 kV. Holey carbon grids (400 mesh) were purchased from Agar Scientific and prepared by diluting dispersion to a low concentration and drop casting onto a grid placed on filter paper to wick away excess surfactant/water. Flake dimensions were obtained by measuring the longest axis of the nanosheet and assigning it "length" then measuring an axis perpendicular to this at its widest point and assigning it "width".

Atomic force microscopy (AFM) was carried out on a Veeco Nanoscope-IIIa (Digital Instruments) system equipped with a E-head (13 μm scanner) in tapping mode after depositing a drop of the dispersion (10 μL) on a preheated (100 °C) Si/SiO$_2$ wafer with an oxide layer of 300 nm. After deposition, the wafer was soaked in Millipore water overnight and rinsed with 5 mL of water and 5 mL of isopropyl alcohol prior to imaging to remove the majority of surfactant. Typical image sizes were 2.5−5 μm at scan rates of 0.4−0.6 Hz. The measured apparent thickness was converted into a number of layers using the known step height of an individual nanosheet as previously reported.[39]

Scanning electron microscopy was performed on shear exfoliated MoS$_2$ film using Carl Zeiss Ultra microscope operated at 10 kV to acquire the secondary electron images of sample. Samples were prepared by vacuum filtration of shear exfoliated MoS$_2$ dispersion (mixed under standard conditions) using 20 nm pore size alumina membranes (Whatman Inc.). The films were dried under vacuum at 60 °C overnight. A small piece of this exfoliated MoS$_2$ on alumina was placed on carbon tab to visualize flakes under SEM.

Raman spectroscopy was performed using a Horiba Jobin Yvon LabRAM HR800 with 532 nm excitation laser in air under ambient conditions. The Raman emission was collected by 100× objective lens (N.A. = 0.8) and dispersed by 600 g/mm. To avoid sample heating we carried out all Raman experiments at 10% of maximum laser power (<5 mW). The samples for Raman spectroscopy were prepared by vacuum filtering the exfoliated MoS$_2$ dispersions on alumina membranes, as described above.

HER Electrode Preparation. We found the high surfactant concentrations to significantly inhibit film formation and transfer. We have thus applied a second centrifugation step to remove the free surfactant after the standard centrifugation at 1,500 rpm. After our second high-speed centrifugation (180 min, 11,000 rpm = 13,250 g, Heraeus Megafuge 16 benchtop centrifuge, Fiberlite rotor F15-6 × 100), the supernatant was discarded, and the sediment was redispersed in the same volume of aqueous SC solution with a concentration of 2 mg/mL. The mean length and thickness was determined according to the extinction spectra metrics as described in the main text.

Dispersions of MoS$_2$ in water/surfactant were vacuum-filtered using porous cellulose filter membranes (MF-Millipore membrane, mixed cellulose esters, hydrophilic, 0.025 μm) to give uniform thin films. The deposited films were then cut into pieces (0.65 cm^2) and transferred on pyrolytic carbon (PyC) electrodes via a normal transferring method. The cellulose filter membrane was then removed by treatment with acetone vapor and subsequent acetone liquid baths followed by isopropyl alcohol rinse to remove the acetone residual. The mass per area for all samples was approximately 0.15 mg/cm^2.

The pyrolytic carbon (PyC) was grown by CVD of acetylene at 950 °C for 30 min to a thickness of 300−400 on 300 nm thermal SiO$_2$ on Si substrates in a hot wall quartz tube furnace as previously reported.[58]

Following CVD of PyC, the samples were cooled under Ar atmosphere to room temperature.

Electrochemical Characterization. Electrochemical measurements were carried out to evaluate the performance of shear-exfoliated MoS$_2$ as electrodes for HER. The measurements were performed in 0.5 M H$_2$SO$_4$ solution using a three-electrode electrochemical cell, with a reversible hydrogen electrode (RHE) reference electrode and graphite rod counter electrode. Electrochemical tests consisted of linear sweep voltammetry and electrochemical impedance spectroscopy using Gamry Reference 3000 potentiostat. The electrocatalysis was measured using linear sweeping from 0 V to −0.9 V (vs RHE) with a scan rate of 5 mV/S. The AC impedance is measured within the frequency range of 0.1 to 10 mHz with perturbation voltage amplitude of 10 mV. The equivalent series resistance of the system was measured by impedance spectroscopy from the high frequency intercept with the real impedance axis, and all the data were corrected by iR compensation.

■ ASSOCIATED CONTENT

ⓢ Supporting Information

Details of speed control and measurement systems. TEM of WS$_2$ and BN nanosheets. Stability of electrocatalytic MoS$_2$ films. This material is available free of charge via the Internet at http://pubs.acs.org.

■ AUTHOR INFORMATION

Corresponding Author
*E-mail: colemaj@tcd.ie.

Notes

The authors declare no competing financial interest.

■ ACKNOWLEDGMENTS

■ REFERENCES

(1) Geim, A. K. *Science* 2009, 324, 1530−1534.
(2) Novoselov, K. S.; Fal'ko, V. I.; Colombo, L.; Gellert, P. R.; Schwab, M. G.; Kim, K. *Nature* 2012, 490, 192−200.
(3) Chhowalla, M.; Shin, H. S.; Eda, G.; Li, L. J.; Loh, K. P.; Zhang, H. *Nat. Chem.* 2013, 5, 263−275.
(4) Wang, Q. H.; Kalantar-Zadeh, K.; Kis, A.; Coleman, J. N.; Strano, M. S. *Nat. Nanotechnol.* 2012, 7, 699−712.
(5) Balendhran, S.; Walia, S.; Nili, H.; Ou, J. Z.; Zhuiykov, S.; Kaner, R. B.; Sriram, S.; Bhaskaran, M.; Kalantar-zadeh, K. *Adv. Funct. Mater.* 2013, 23, 3952−3970.
(6) Coleman, J. N.; Lotya, M.; O'Neill, A.; Bergin, S. D.; King, P. J.; Khan, U.; Young, K.; Gaucher, A.; De, S.; Smith, R. J.; Shvets, I. V.; Arora, S. K.; Stanton, G.; Kim, H. Y.; Lee, K.; Kim, G. T.; Duesberg, G. S.; Hallam, T.; Boland, J. J.; Wang, J. J.; Donegan, J. F.; Grunlan, J. C.; Moriarty, G.; Shmeliov, A.; Nicholls, R. J.; Perkins, J. M.; Grieveson, E. M.; Theuwissen, K.; McComb, D. W.; Nellist, P. D.; Nicolosi, V. *Science* 2011, 331, 568−571.
(7) Nicolosi, V.; Chhowalla, M.; Kanatzidis, M. G.; Strano, M. S.; Coleman, J. N. *Science* 2013, DOI: 10.1126/science.1226419.
(8) Hernandez, Y.; Nicolosi, V.; Lotya, M.; Blighe, F. M.; Sun, Z.; De, S.; McGovern, I. T.; Holland, B.; Byrne, M.; Gun'Ko, Y. K.; Boland, J.

J.; Niraj, P.; Duesberg, G.; Krishnamurthy, S.; Goodhue, R.; Hutchison, J.; Scardaci, V.; Ferrari, A. C.; Coleman, J. N. *Nat. Nanotechnol.* **2008**, *3*, 563−568.

(9) Coleman, J. N. *Acc. Chem. Res.* **2013**, *46*, 14−22.

(10) Zhou, K. G.; Mao, N. N.; Wang, H. X.; Peng, Y.; Zhang, H. L. *Angew. Chem., Int. Ed.* **2011**, *50*, 10839−10842.

(11) Yi, M.; Shen, Z.; Zhang, X.; Ma, S. *J. Phys. D: Appl. Phys.* **2013**, *46*, 025301.

(12) Lotya, M.; Hernandez, Y.; King, P. J.; Smith, R. J.; Nicolosi, V.; Karlsson, L. S.; Blighe, F. M.; De, S.; Wang, Z.; McGovern, I. T.; Duesberg, G. S.; Coleman, J. N. *J. Am. Chem. Soc.* **2009**, *131*, 3611−3620.

(13) Smith, R. J.; King, P. J.; Lotya, M.; Wirtz, C.; Khan, U.; De, S.; O'Neill, A.; Duesberg, G. S.; Grunlan, J. C.; Moriarty, G.; Chen, J.; Wang, J.; Minett, A. I.; Nicolosi, V.; Coleman, J. N. *Adv. Mater. (Weinheim, Ger.)* **2011**, *23*, 3944−3948.

(14) Wang, S.; Yi, M.; Shen, Z.; Zhang, X.; Ma, S. *RSC Adv.* **2014**, *4*, 25374−25378.

(15) May, P.; Khan, U.; Hughes, J. M.; Coleman, J. N. *J. Phys. Chem. C* **2012**, *116*, 11393−11400.

(16) May, P.; Khan, U.; O'Neill, A.; Coleman, J. N. *J. Mater. Chem.* **2012**, *22*, 1278−1282.

(17) Hughes, J. M.; Aherne, D.; Coleman, J. N. *J. Appl. Polym. Sci.* **2013**, *127*, 4483−4491.

(18) Israelachvili, J. N. *Intermolecular and Surface Forces*; Academic Press: 2011.

(19) Bourlinos, A. B.; Georgakilas, V.; Zboril, R.; Steriotis, T. A.; Stubos, A. K. *Small* **2009**, *5*, 1841−1845.

(20) Zhi, C. Y.; Bando, Y.; Tang, C. C.; Kuwahara, H.; Golberg, D. *Adv. Mater. (Weinheim, Ger.)* **2009**, *21*, 2889−2893.

(21) Cunningham, G.; Lotya, M.; Cucinotta, C. S.; Sanvito, S.; Bergin, S. D.; Menzel, R.; Shaffer, M. S. P.; Coleman, J. N. *ACS Nano* **2012**, *6*, 3468−3480.

(22) O'Neill, A.; Khan, U.; Coleman, J. N. *Chem. Mater.* **2012**, *24*, 2414−2421.

(23) Khan, U.; O'Neill, A.; Lotya, M.; De, S.; Coleman, J. N. *Small* **2010**, *6*, 864−871.

(24) Finn, D. J.; Lotya, M.; Cunningham, G.; Smith, R. J.; McCloskey, D.; Donegan, J. F.; Coleman, J. N. *J. Mater. Chem. C* **2014**, *2*, 925−932.

(25) Torrisi, F.; Hasan, T.; Wu, W.; Sun, Z.; Lombardo, A.; Kulmala, T. S.; Hsieh, G.-W.; Jung, S.; Bonaccorso, F.; Paul, P. J.; Chu, D.; Ferrari, A. C. *ACS Nano* **2012**, *6*, 2992−3006.

(26) Wang, J. Z.; Lu, L.; Lotya, M.; Coleman, J. N.; Chou, S. L.; Liu, H. K.; Minett, A. I.; Chen, J. *Adv. Energy Mater.* **2013**, *3*, 798−805.

(27) Alsaif, M. M. Y. A.; Latham, K.; Field, M. R.; Yao, D. D.; Medehkar, N. V.; Beane, G. A.; Kaner, R. B.; Russo, S. P.; Ou, J. Z.; Kalantar-zadeh, K. *Adv. Mater. (Weinheim, Ger.)* **2014**, *26*, 3931−3937.

(28) Cunningham, G.; Khan, U.; Backes, C.; Hanlon, D.; McCloskey, D.; Donegan, J.; Coleman, J. N. *J. Mater. Chem. C* **2013**, *1*, 6899−6904.

(29) Cunningham, G.; Hanlon, D.; McEvoy, N.; Duesberg, G. S.; Coleman, J. N. *Nanoscale* **2015**, *7*, 198−208.

(30) Kavan, L.; Yum, J. H.; Graetzel, M. *ACS Nano* **2011**, *5*, 165−172.

(31) Feng, J.; Sun, X.; Wu, C.; Peng, L.; Lin, C.; Hu, S.; Yang, J.; Xie, Y. *J. Am. Chem. Soc.* **2011**, *133*, 17832−17838.

(32) Bang, G. S.; Nam, K. W.; Kim, J. Y.; Shin, J.; Choi, J. W.; Choi, S.-Y. *ACS Appl. Mater. Interfaces* **2014**, *6*, 7084−7089.

(33) Ji, S.; Yang, Z.; Zhang, C.; Liu, Z.; Tjiu, W. W.; Phang, I. Y.; Zhang, Z.; Pan, J.; Liu, T. *Electrochim. Acta* **2013**, *109*, 269−275.

(34) Chen, X. J.; Dobson, J. F.; Raston, C. L. *Chem. Commun. (Cambridge, U. K.)* **2012**, *48*, 3703−3705.

(35) Paton, K. R.; Varrla, E.; Backes, C.; Smith, R. J.; Khan, U.; O'Neill, A.; Boland, C.; Lotya, M.; Istrate, O. M.; King, P.; Higgins, T.; Barwich, S.; May, P.; Puczkarski, P.; Ahmed, I.; Moebius, M.; Pettersson, H.; Long, E.; Coelho, J.; O'Brien, S. E.; McGuire, E. K.; Mendoza-Sanchez, B.; Duesberg, G. S.; McEvoy, N.; Pennycook, T. J.; Downing, C.; Crossley, A.; Nicolosi, V.; Coleman, J. N. *Nat. Mater.* **2014**, *13*, 624−630.

(36) Liu, L.; Shen, Z.; Yi, M.; Zhang, X.; Ma, S. *RSC Adv.* **2014**, *4*, 36464−36470.

(37) Varrla, E.; Paton, K. R.; Backes, C.; Harvey, A.; Smith, R. J.; McCauley, J.; Coleman, J. N. *Nanoscale* **2014**, *6*, 11810−11819.

(38) Yi, M.; Shen, Z. G. *Carbon* **2014**, *78*, 622−626.

(39) Backes, C.; Smith, R. J.; McEvoy, N.; Berner, N. C.; McCloskey, D.; Nerl, H. C.; O'Neill, A.; King, P. J.; Higgins, T.; Hanlon, D.; Scheuschner, N.; Maultzsch, J.; Houben, L.; Duesberg, G. S.; Donegan, J. F.; Nicolosi, V.; Coleman, J. N. *Nat. Commun.* **2014**, *5*, 4576.

(40) Khan, U.; O'Neill, A.; Porwal, H.; May, P.; Nawaz, K.; Coleman, J. N. *Carbon* **2012**, *50*, 470−475.

(41) Jaramillo, T. F.; Jorgensen, K. P.; Bonde, J.; Nielsen, J. H.; Horch, S.; Chorkendorff, I. *Science* **2007**, *317*, 100−102.

(42) Green, A. A.; Hersam, M. C. *Nano Lett.* **2009**, *9*, 4031−4036.

(43) Vadukumpully, S.; Paul, J.; Valiyaveettil, S. *Carbon* **2009**, *47*, 3288−3294.

(44) Smith, R. J.; Lotya, M.; Coleman, J. N. *New J. Phys.* **2010**, *12*, 125008.

(45) Hunter, R. J. *Foundations of Colloid Science*; OUP: Oxford, 2001.

(46) Chou, S. S.; De, M.; Kim, J.; Byun, S.; Dykstra, C.; Yu, J.; Huang, J.; Dravid, V. P. *J. Am. Chem. Soc.* **2013**, *135*, 4584−4587.

(47) Lee, C.; Yan, H.; Brus, L. E.; Heinz, T. F.; Hone, J.; Ryu, S. *ACS Nano* **2010**, *4*, 2695−2700.

(48) Jimenez Sandoval, S.; Yang, D.; Frindt, R. F.; Irwin, J. C. *Phys. Rev. B: Condens. Matter* **1991**, *44*, 3955−62.

(49) Li, H.; Zhang, Q.; Yap, C. C. R.; Tay, B. K.; Edwin, T. H. T.; Olivier, A.; Baillargeat, D. *Adv. Funct. Mater.* **2012**, *22*, 1385−1390.

(50) Yadgarov, L.; Choi, C. L.; Sedova, A.; Cohen, A.; Rosentsveig, R.; Bar-Elli, O.; Oron, D.; Dai, H.; Tenne, R. *ACS Nano* **2014**, *8*, 3575−3583.

(51) Wilson, J. A.; Yoffe, A. D. *Adv. Phys.* **1969**, *18*, 193−335.

(52) Hanlon, D.; Backes, C.; Hughes, M.; O'Neill, A.; King, P.; Higgins, T.; McEvoy, N.; Duesberg, G. S.; Mendoza-Sanchez, B.; Nicolosi, V.; Coleman, J. N. *Chem. Mater.* **2013**, *26*, 1751−1763.

(53) Holland, F. A. *Fluid Flow for Chemical Engineers*; Chemical Publishing Company: 1973.

(54) Holland, F. A.; Chapman, F. S. *Liquid mixing and processing in stirred tanks*; Reinhold Pub. Corp: 1966.

(55) Winchester, A.; Ghosh, S.; Feng, S. M.; Elias, A. L.; Mallouk, T.; Terrones, M.; Talapatra, S. *ACS Appl. Mater. Interfaces* **2014**, *6*, 2125−2130.

(56) Voiry, D.; Salehi, M.; Silva, R.; Fujita, T.; Chen, M.; Asefa, T.; Shenoy, V. B.; Eda, G.; Chhowalla, M. *Nano Lett.* **2013**, *13*, 6222−6227.

(57) Voiry, D.; Yamaguchi, H.; Li, J.; Silva, R.; Alves, D. C. B.; Fujita, T.; Chen, M.; Asefa, T.; Shenoy, V. B.; Eda, G.; Chhowalla, M. *Nat. Mater.* **2013**, *12*, 850−855.

(58) McEvoy, N.; Peltekis, N.; Kumar, S.; Rezvani, E.; Nolan, H.; Keeley, G. P.; Blau, W. J.; Duesberg, G. S. *Carbon* **2012**, *50* (3), 1216−1226.